Imaging confined and bulk p-type/n-type carriers in (Al,Ga)N heterostructures with multiple quantum wells

A. Minj[1,2]*, M. Zhao[1], B. Bakeroot[3], K. Paredis[1]

[1]*IMEC, Kapeldreef 75, 3001 Leuven, Belgium*
[2]*Quantum Solid-State Physics, KU Leuven, Celestijnenlaan 200D, 3001 Leuven, Belgium*
[3]*Centre for Microsystems Technology (CMST), imec and Ghent University, Technologiepark 126, 9052 Gent, Belgium*

*email: albert.minj@imec.be

ABSTRACT

Current state of dopant assessment for the optimization of the III-nitride-based heterostructures for high frequency, high power and light emission applications relies heavily on quantitative chemical analysis techniques. In such complex heterostructures, determination of P-type carrier density of the cap layer, control of background concentration and assessment of polarization induced confined carriers are necessary for the realization of optimal devices. None of these can be completely inferred from chemical analysis owing to several material and growth issues including poor activation of Mg, presence of O impurities and amphoteric nature of carbon impurities. Here, as regions of interest require nanometre resolution, especially near the interfaces featuring triangular quantum wells and exhibiting electron/hole confinement, exploitation of the behaviour of nano-size metal-semiconductor junction formed between metallic scanning probe microscopy probe and III-nitride surface is promising for carrier determination. By combining two techniques sensitive to local change in capacitance and rectifying characteristic of conduction at the nanoscale, the nature of free carriers originating from extrinsic n-type and p-type dopants and polarization induced confined carriers, two-dimensional electron gas and hole gas, were eventually revealed across III-nitride heterostructures.

With ever increasing demand for low-power consuming devices and diminishing returns of performance over cost of investment in Si-technology, the advances in wafer-scale epitaxy in the past decade have eventually put III-nitrides (III-N) in a pivotal role for optoelectronics and power applications [1]. However, the current progress in III-N device technology is facing doping and material characterization issues. For example, the high p-type doping of the GaN cap layer required

for bringing the high electron mobility transistors (HEMTs) in the normally-OFF mode [2] is hindered by a poor activation of Mg dopants in the metal-organic chemical vapor deposition reactors [3,4]. Additionally, there is also a pressing need to control background or unintentional carrier concentration that is originating from impurities and point defects in the channel [5–7] to reduce device leakage, which has led to doping by compensating centers like carbon [8]. Even though the concentration of constituent dopants can be determined from secondary ion mass spectroscopy, establishing their ionization is not straightforward owing to a strong influence on Mg activation from unwanted impurities like hydrogen and oxygen [4], and dopants like C acting as both donor and compensation centers depending on their substitutional site belonging to the group III or N it occupies [7–9]. Even the AlGaN transition layers (TLs) used for quality growth of GaN layer on Si substrate needs optimal design as polarization induced hole doping near the GaN/AlGaN interface can provide control over short channel effects [10]. Furthermore, not limiting to single channel HEMTs, the design of double channel HEMTs, which alleviates current collapse issues and allows linearity enhancement [11] could gain from the robust characterization of the two channels. Therefore, to realize better design of devices, not only chemical doping but also polarization induced carriers across the device stack need to be accounted for. In this regard, robust and reliable carrier characterization in epilayers and at interfaces with applicability to device dimensions are a necessity.

Scanning probe microscopy (SPM) methodologies, such as Scanning spreading resistance microscopy (SSRM) [12] and Scanning capacitance microscopy (SCM) [13], which are sensitive to local charges and offer the needed resolution, have been exploited to study narrow band gap semiconductors such as Si, SiGe, InP, GaAs etc., where conventional adhesive Ag or Ga-In eutectic offer acceptable low resistance back contact [14]. They have also been explored on wide band gap SiC [15–20] with fabricated back contacts. Early assessment of SSRM/SCM techniques for (Al,Ga,In)N alloys done by R.A. Oliver et al. suggests that the main challenges are the surface charging effects and high resistivity requiring application of high DC and AC bias for detectable SCM signal, casting doubt at the reliability and repeatability of such kind of measurements [21]. Nevertheless, SCM analysis has been used to investigate depth-distribution and activation of Mg and unintentionally doped regions formed during the coalescence stage of epitaxial lateral overgrowth [22], implanted ions [23] and n-type compensation during thermal oxidation [24], and has also allowed for determination of threshold voltage and barrier thickness variation in AlGaN/GaN heterostructure [25,26]. A. Imtiaz et al. correctly identified P-type and N-type regions

in single GaN nanowire PN junction by detecting microwave reflection S_{11}' in Scanning Microwave Microscopy (**SMM**) but required much higher measurement frequencies (18.5 GHz) than commercial modules [27]. Recently, Srividov et al. successfully demonstrated direct imaging of confined carriers in the III-N quantum wells by SSRM at low DC bias, which restate the high potential of such techniques [28]. In this paper, we revisit the two techniques, Conductive-Atomic force microscopy (C-AFM) and SCM, for application in characterization of doping in wide band III-N.

Three samples consisting of p++ GaN/p-GaN/AlN (5 nm), n-GaN layer (1.7 μm) and n++GaN layer (500 nm) heterostructures grown by metal organic vapor phase epitaxy (MOVPE) on an undoped GaN buffer were investigated. 200 nm thick AlN and $Al_{0.75}Ga_{0.25}N/Al_{0.44}Ga_{0.56}N/Al_{0.08}Ga_{0.92}N$ stack served as the nucleation layer and the transition layers, respectively, for the growth of the GaN buffer on a Si<111> substrate. Their structural description is schematically detailed in Figure 1. Room temperature electron/hole mobility and the free carrier concentration in the doped layers as determined from Hall measurement are presented in Table 1.

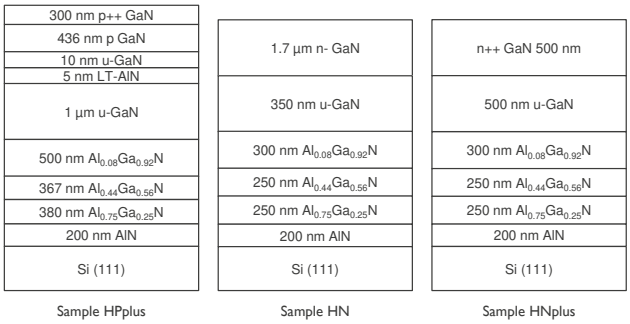

Figure 1: Structural detail of samples HPplus, HN and HNplus.

	p++ GaN (HPplus)	**n-GaN (HN)**	**n++ GaN (HNplus)**
n/p (cm^{-3})	$4.11x10^{17}$	$4.51x10^{16}$	$1.38x10^{19}$
μ ($cm^{-2}/V-s$)	~16	~458	~59

Table 1: Free carrier concentration and Hall mobility in the top GaN layer in samples HPplus, HN and HNplus.

Local conductivity and carrier type assessment were carried out in C-AFM mode implemented on *Bruker Dimension ICON* AFM in dry environment (Ar-filled glove box at >1 bar) and in the SCM mode on a *Park Systems NX-Hivac* AFM in high-vacuum (~ 2-5×10^{-5} torr). Commercial pure Pt/Ir probe with nominal spring constant k ~ 26 N/m were used for C-AFM and Pt/Ir coated Si AFM probes with k ~ 3 N/m and tip radius < 25 nm for SCM measurements. In the former method, current is acquired through a current amplifier (sensitivity of ~1 pA) as the AFM probe (ground) scans over the DC biased sample surface. Here, the spatial resolution will be defined by tip-sample contact area [29]. The second method SCM is sensitive to the modulation in tip-sample capacitance $^{dC}/_{dV}$ induced by small external AC bias. It employs an ultra-high frequency capacitance sensor; ~1 GHz oscillator coupling the resonator with a RF power detection circuit. Any change in the tip-sample capacitance affects the resonance characteristic of the resonator and is detected via lock-in amplifier (AC bias of 0.5 - 1.0 V at 17 kHz to the sample) as amplitude and the phase. dC/dV has been demonstrated to be sensitive to the carried density in the range 5x**10^{15}**– 8x10^{19} **cm^{-3}** (5x10^{14}-2x10^{19} **cm^{-3}**) for p-type (n-type) silicon [30]. Unlike C-AFM, the spatial resolution of SCM is poor (> 25 nm) as it is limited by parasitic capacitance of the conical shape of the AFM probe [31].

Ti/Al-based back contacts were fabricated on the freshly cleaved cross-section of the heterostructures. Its optimization was initially carried out on the undoped 70 nm-thick AlGaN (0001) layer, where rapid thermal annealing of the sputtered Ti/Al at 825 °C for 15 s in 1 bar N_2 atmosphere yielded linear current-voltage behaviour (see Figure S1 in supporting information).

Owing to the polarization gradient $\nabla . P$ at the interface between two adjacent nitride layers, strong polarization charges with contributions from spontaneous and piezoelectric polarization are formed. Accordingly, this can lead to redistribution of carriers and formation of either two-dimensional electron gas (2DEG) or hole gas (2DHG). Therefore, the electron density and band edges were simulated for fully strained heterostructures using TCAD simulation. The calculated band edges in Figure 2 show that the Fermi-level in all three heterostructures is situated very close to the valence band at the two $Al_xGa_{1-x}N/Al_yGa_{1-y}N$ ($x \neq y$) interfaces of the transition layers (marked as 1 and 2 in

the figure) and also at undoped GaN buffer/AlGaN interface (marked as 3). This is indeed the case as negative polarization charges are formed at the aforementioned $Al_xGa_{1-x}N/Al_yGa_{1-y}N$ interface (where $x < y$) accumulating holes in its proximity. The 2DHG near the two interfaces in the transition layers and the u-GaN/AlGaN interface is observed in the calculated hole density profiles across these interfaces (see Figure 2b). Due to high density of threading dislocations, a complete strain relaxation in the transition layers is expected. That is why, even though in the calculation the hole densities at interfaces 1 and 2 of the transition layers is almost 10x of the GaN buffer/AlGaN interface, in the electrical measurements, which will be discussed later, the two interfaces show diminished conductivity and SCM signal indicative of the low carrier density. One can also see that for all the heterostructures, a strong built-in field is formed in the GaN buffer layer, which typically results from the formation of the junction with the overgrown n-GaN (sample HN) and n+ GaN (sample HNplus) layers and from the presence of positive polarization charges at its interface with 5 nm AlN (sample HPplus). The depletion region or space charge region (SCR) is mainly formed in the GaN buffer because of its undoped nature. For the HPplus sample, there are two additional interfaces, AlN (5 nm)/ u-GaN buffer with positive polarization charge density and u-GaN (10 nm)/AlN (5 nm) with negative polarization charge density. The simulation (see Figure 2b) confirms that they respectively allow formation of 2DEG and 2DHG near the interfaces too.

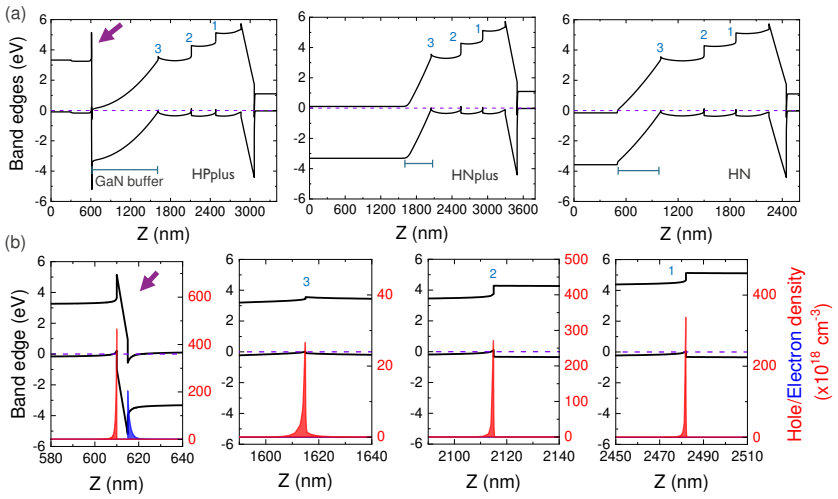

Figure 2: (a) Calculated band diagrams across the heterostructure of samples HPplus, HNplus and HN featuring three common interfaces marked as 1, 2 and 3 in addition to u-GaN (10 nm)/AlN (5 nm)/u-GaN structure specific to HPplus sample indicated by an arrow. They are magnified in (b). GaN buffer layers are indicated as horizontal bars. (b) Band edges and electron/hole density profiles in sample HPplus with a higher magnification across u-GaN buffer/$Al_{0.08}Ga_{0.92}N$ (marked as 3), $Al_{0.08}Ga_{0.92}N/Al_{0.44}Ga_{0.56}N$ (marked as 2) and $Al_{0.44}Ga_{0.56}N/Al_{0.75}Ga_{0.25}N$ (marked as 1) structures and at u-GaN/AlN/u-GaN buffer structure (indicated by arrow). The hole density is plotted in solid red and electron density in blue line.

Both the extrinsic and polarization-induced carriers across the III-N stack can be analysed from the dependence of diode-behaviour of the tip-sample junction on carrier type and density, either in terms of conduction or capacitance. To ensure that local current transport is dominated by only one type of carriers, the polarity of sample bias was accordingly chosen to keep the tip-sample junction in forward bias. As the probe is electrically grounded in the C-AFM measurements, positive (negative) DC bias to the sample corresponds to a forward bias condition in the p-type (n-type) region. C-AFM map obtained at positive DC bias, which serves as the forward bias for the tip/p-type (Al,Ga)N junction, shows higher conduction around the two interfaces of the transition layers where 2DHGs are located (shown for sample HPplus at +2.5 V bias in **Figure 3a**), while for negative DC bias there is no measurable conduction due to the reverse bias condition (see C-AFM map -2 V in **Figure 3b**). The patchy current distribution along the interfaces is due to the poor morphology of the cleaved surface, which can also be seen in Figure 3a-c. This issue was resolved by using sharp full diamond tip (FDT) probes [32] through which a higher pressure can be applied to improve the tip-sample contact (see C-AFM maps obtained at -2 V and 3 V using FDT probes in Figure S6). Local position of current paths can be inferred from the schematic of sample HPplus cross-section provided in **Figure 3d** in the right scale. Interestingly for sample HPplus, higher conduction is indistinguishably observed at either or both interfaces in u-GaN/AlN/buffer-GaN for both DC polarities. As the two interfaces are only separated by 5 nm, electron- and hole-dominated current paths via 2DEG and 2DHG, respectively, cannot be resolved from two consecutively obtained maps due to thermal drift of the closed-loop scanner. To circumvent this issue, a measurement was carried out with consecutive segments of the same scan probed with DC bias of alternating polarity ($-2.0\ \mathrm{V} \rightarrow +2.5\ \mathrm{V} \rightarrow -2.0\ \mathrm{V} \rightarrow +2.5\ \mathrm{V} \rightarrow -2.5\ \mathrm{V} \rightarrow 3.0\ \mathrm{V} \rightarrow -2.5\ \mathrm{V} \rightarrow +3.0\ \mathrm{V}$) one after the other. This revealed both electron- and hole-dominated conduction regions with spatial information in a single scan current map. As per the bias pattern, it allowed conductivity mapping with segments of alternatingly electron- and hole-

dominated conduction, which is presented in **Figure 3c**. It can be observed that right at the transition from one segment to the other, separate conduction paths associated to 2DEG and 2DHG regions are reliably resolved. In general, this is apparent in the current profile in **Figure 3f**, however, the two conduction paths overlap over a region width of ~36 nm. This is most likely a resolution issue of the AFM probe used. For increasing forward bias reaching -2.5V, gradual smearing of conduction occurs in u-GaN towards interface 3, which is absent in positive bias, thus validating the n-type nature of u-GaN layer as well. The rectifying behaviour in the local current-voltage (I-V) characteristics also confirms the Schottky-type tip-sample junction formed on N-type region near 2DEG and P-type near 2DHG interfaces (see **Figure 3e**). The extracted ideality factor of the tip-sample contact is between 2.5 and 3. This behaviour can be attributed to surface states and interfacial native oxide layer.

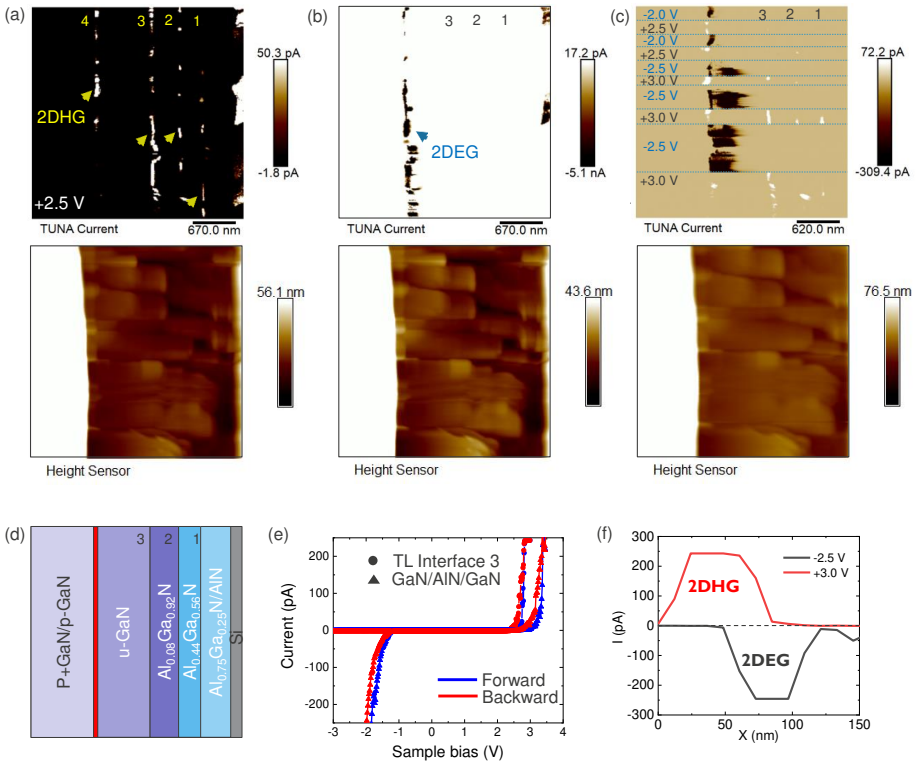

Figure 3: C-AFM maps along with their respective topography below over the same area at sample DC bias of (a) +2.5 V and (b) -2.0 V and (c) for alternating biases with opposite polarity. (d) Schematic of the cross-section

with the same scale as that of CAFM maps in a, b and c except for u-GaN(10 nm)/AlN(5 nm) bilayer (represented with solid red-filled area) which has been expanded for better visibility. (e) Local rectifying I-V profiles at interfaces 3 and 4. (f) Current profile across the u-GaN(10 nm)/AlN(5 nm)/GaN buffer.

The type of the carriers was confirmed by analysing the phase of dC/dV in scanning capacitance microscopy. In a nutshell, dC/dV is positive/negative if the width of junction under the tip decreases/increases with bias V, and it is again dopant dependent. At 0 V bias, the Pt/Ir probe in contact with the surface naturally forms a metal-insulator-semiconductor (MIS) junction on both n- and p-type regions in the presence of native oxide. Except for In-rich III-N, the near surface region is usually depleted in (Al,Ga)N [33,34]. Non-zero dC/dV is observed near the two interfaces of the transition layers in all the three samples (see supporting information Figure S8-S10) and near the u-GaN/AlGaN interface for sample HPplus. In the dC/dV amplitude map for sample HPplus shown in **Figure 4a (**see its simultaneously acquired topography in Figure S7**)**, non-zero dC/dV additionally appears in the top p+/p-GaN bilayer and near the GaN/AlN/buffer-GaN interfaces. The dC/dV phase directly confirms the p-type behaviour with a phase of ~25° at the Mg-doped GaN layers and near regions with a 2DHG and n-type behaviour with an additional phase-shift of 180° near the 2DEG region of the AlN/GaN buffer. Interestingly, as can be seen from the profile across the heterostructure, dC/dV gradually drops within ~128 nm in the p-GaN layer (encircled in **Figure 4d**) from the u-GaN/AlN interface. One may picture it this way: when the AFM tip is over the negative SCR of 2DHG near the u-GaN/AlN interface, the AC bias will additionally modulate the positive SCR of the 2DEG region situated just 5 nm from negative SCR but with 180° phase-shift. Thus, dC/dV drop is due to the subtractive nature of the positive SCR in the vicinity to the net value, which only reveals the susceptibility of the SCM to a convolution of two opposite SCR regions in proximity. In the region with undetectable dC/dV (for e.g., u-GaN, AlGaN), amplitude is obviously zero and phase fluctuates between -180° and 180° seamless texture with noise effect contrast. All N-type regions (interfaces with 2DEG, n-GaN layer in sample HN and n++ GaN in sample HNplus) enhance and all p-type regions (near interfaces 1, 2 and 3 and Mg-doped GaN layer) deplete at -2 V (**Figure 4b**) and vice-versa is true for 2 V (**Figure 4c**). See Figures S9 and S10 to see this trend in samples HN and HNplus. With 2DEG region depleting completely at 2 V, the 2DHG associated with the adjacent interface could be eventually be revealed.

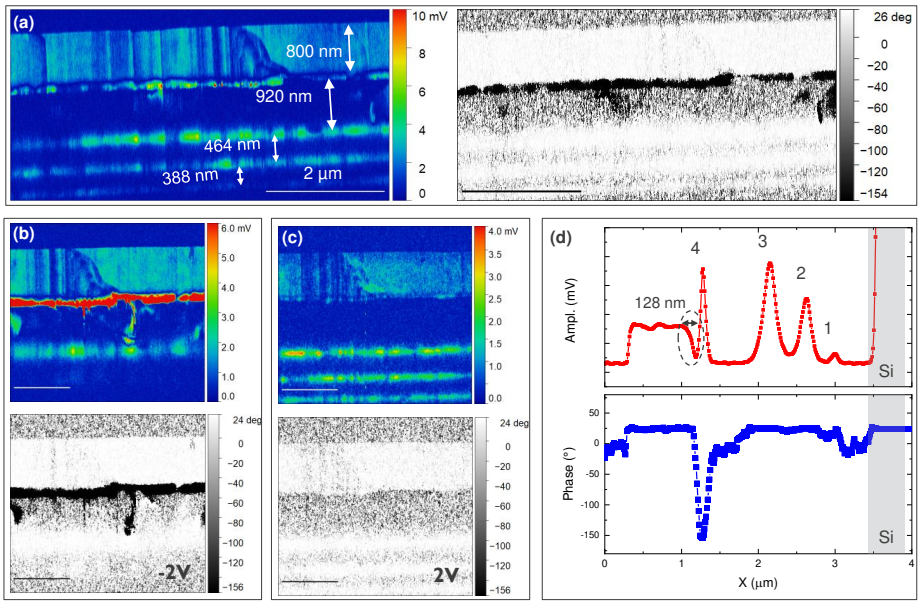

Figure 4: (Sample HPplus) dC/dV amplitude in color scale and phase maps in gray scale for (a) DC bias = 0V (a), (b) -2 V and (c) 2V. (d) Average dC/dV profile across the heterostructure at 0V. The scale bars in (b) and (c) is 1 µm.

The efficacy of Ti/Al-based back-contact for C-AFM and SCM measurements was better than that of indium and Ag paste back contacts. This was assessed by comparing the magnitude of current and dC/dV on samples HN and HPplus, respectively. For this purpose, pure Pt/Ir probes were used to avoid tip degradation over time in order to carry out fair comparison. In C-AFM analysis, the DC bias was adjusted to keep the current at u-GaN/AlGaN1 interface of sample HN in the range 0.6 - 0.8 nA. To reach this range, while 4 V was sufficient for Ti/Al back contact, a much higher bias, 5 V - 5.5 V, was required for indium contact (see **Figure 5a**). And almost no current was measured within the detection limit of ~ 1 pA when Ag paste was used. From the comparison of average dC/dV profiles on sample HPplus obtained at 2 V over four successive scans (**Figure 5b**), one can see that dC/dV amplitude is overall higher for Ti/Al-based contact than for the other two, which is clear on p-GaN layer and on two of the three interfaces with 2DHGs. dC/dV at u-GaN/AlGaN1 interface for Ti/Al-case is only comparable to that of Indium and Ag paste, which is strictly due to poor tip-sample

contact in the presence of step-like morphology around this interface. The repeatability of these measurements up to 4 successive scans also eliminates any indication of significant tip-degradation. A full description of the experiments is provided in the supporting information section 2 (see Figure S3-S5).

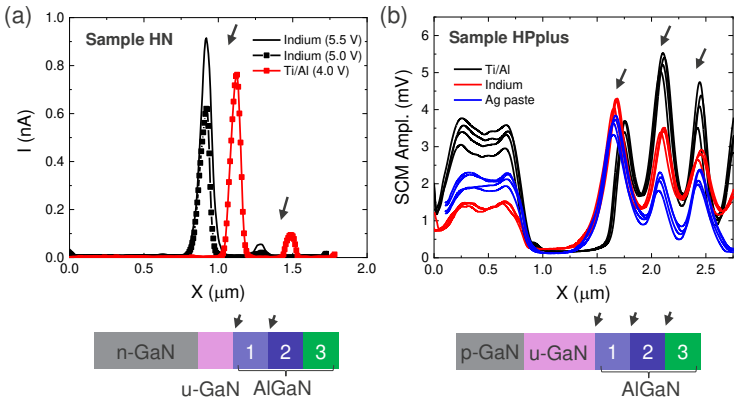

Figure 5: (a) Average current profiles at varying sample bias and (b) average dC/dV profiles at 2 V over four successive measurements of the same area across the III-N stack in sample HN and HPplus, respectively, for three types of back contacts. The current profiles related to Ti/Al and indium contact are shifted apart in (a) for better view. The arrows in the graphs are indicative of the concerned interfaces schematically shown below.

Two scanning probe microscopy methodologies, C-AFM and SCM, commonly used for the characterization of narrow band gap semiconductor structures and capable of reaching nanometer resolution were revisited for their applicability on III-N heterostructures with wide band gap larger than 3.4 eV. Ti/Al-based contacts were implemented on the cross-section to reduce the impact of back contact resistance on local current flow. It additionally resulted in improved dC/dV signal strength when compared to indium and Ag-based back contacts. Lower back contact barrier and reduced surface charging allowed for C-AFM measurements at lower DC biases. Here, charging effect was assessed by continuously scanning the same area and monitoring any observable change in the signal strength [35]. Because of the rectifying property of the tip-sample junction for both n-type and p-type doped (Al,Ga)N regions, through selection of the polarity of the DC bias and conductivity measurement, the type of the doping was identified. Thanks to the small tip-sample

contact area, C-AFM technique eventually allowed resolving the 2DHG and 2DEG regions separated by only 5 nm AlN layer. This illustrates the potential of this technique to be applicable to study device heterostructures for high power and RF applications and multi-quantum well heterostructures as in optoelectronic devices. Large SCM signal strength for AC bias ≤ 1 V was observed on both chemically doped regions and on polarization induced doping regions near the interface. Furthermore, no signal was recorded otherwise on undoped regions as in u-GaN and AlGaN regions in the transition layers. A phase shift of approximately 180° between n-type and p-type regions in SCM phase maps verifies the absolute and correct determination of the type of doping. By probing p-type layer, 2DEG channel and 2DHGs in the TLs of the same heterostructure, C-AFM/SCM proves to be promising methodology for optimizing design of p-GaN HEMT.

Supplementary material provides efficacy of Ti/Al back contact methodology for improved signal in C-AFM/SCM modes, repeatability tests, current maps by FDT probe, and additional SCM results for samples HPlus, HN and HNplus.

ACKNOWLEDGEMENTS

The project has received funding from the European Union's Horizon 2020 research and innovation programme under the Marie Sklodowska-Curie grant agreement No 896390.

DATA AVAILABILITY

The data that support the findings of this study are available from the corresponding author upon reasonable request.

References

[1] F. Ren and J.C. Zolper, *Wide Energy Bandgap Electronic Devic* (World Scientific, 2003).

[2] Y. Uemoto, M. Hikita, H. Ueno, H. Matsuo, H. Ishida, M. Yanagihara, T. Ueda, T. Tanaka, and D. Ueda, IEEE Trans. Electron Devices **54**, 3393 (2007).

[3] S. Zhao and Z. Mi, Crystals **7**, 268 (2017).

[4] D.-H. Youn, M. Lachab, M. Hao, T. Sugahara, H. Takenaka, Y. Naoi, and S. Sakai, Jpn. J.

Appl. Phys. **38**, 631 (1999).

[5] D.D. Koleske, A.E. Wickenden, R.L. Henry, and M.E. Twigg, J. Cryst. Growth **242**, 55 (2002).

[6] J.L. Lyons, A. Janotti, and C.G. Van De Walle, Phys. Rev. B - Condens. Matter Mater. Phys. **89**, 035204 (2014).

[7] M. Matsubara and E. Bellotti, J. Appl. Phys. **121**, 195701 (2017).

[8] B. Rackauskas, M.J. Uren, S. Stoffels, M. Zhao, S. Decoutere, M. Kuball, S. Member, A. Epitaxial, and A.G. Algan-on-si, IEEE Trans. Electron Devices **65**, 1838 (2018).

[9] A.Y. Polyakov and I. Lee, Mater. Sci. Eng. R **94**, 1 (2015).

[10] T. Han, H. Zhao, X. Peng, and Y. Li, Superlattices Microstruct. **116**, 207 (2018).

[11] R. Chu, Y. Zhou, J. Liu, D. Wang, K.J. Chen, and K.M. Lau, IEEE Trans. Electron Devices **52**, 438 (2005).

[12] P. Eyben, T. Janssens, and W. Vandervorst, Mater. Sci. Eng. B Solid-State Mater. Adv. Technol. **124–125**, 45 (2005).

[13] E. Bussmann and C.C. Williams, Rev. Sci. Instrum. **75**, 422 (2004).

[14] R.P. Lu, K.L. Kavanagh, S.J. Dixon-warren, A.J. Springthorpe, R. Streater, and I. Calder, J. Vac. Sci. Technol. B Microelectron. Nanom. Struct. Process. Meas. Phenom. **20**, 1682 (2002).

[15] F. Giannazzo, L. Calcagno, F. Roccaforte, P. Musumeci, F. La Via, and V. Raineri, Appl. Surf. Sci. **184**, 183 (2001).

[16] F. Giannazzo, L. Calcagno, V. Raineri, L. Ciampolini, M. Ciappa, and E. Napolitani, Appl. Phys. Lett. **79**, 1211 (2001).

[17] O. Bowallius, S. Anand, N. Nordell, G. Landgren, and S. Karlsson, Mater. Sci. Semicond. Process. **4**, 209 (2001).

[18] J. Osterman, A. Hallen, and S. Anand, Appl. Phys. Lett. **81**, 3004 (2002).

[19] J. Suda, S. Nakamura, M. Miura, T. Kimoto, and H. Matsunami, Jpn. J. Appl. Phys. **41**, L40 (2002).

[20] L.K. Swanson, P. Fiorenza, F. Giannazzo, A. Frazzetto, and F. Roccaforte, Appl. Phys. Lett. **101**, 193501 (2012).

[21] R.A. Oliver, Reports Prog. Phys. **71**, 076501 (2008).

[22] J. Sumner, R.A. Oliver, M.J. Kappers, and C.J. Humphreys, J. Appl. Phys. **106**, 104503 (2009).

[23] F. Giannazzo, F. Iucolano, F. Roccaforte, L. Romano, M.G. Grimaldi, and V. Raineri, Solid State Phenom. **131–133**, 491 (2008).

[24] F. Roccaforte, F. Giannazzo, F. Iucolano, C. Bongiorno, and V. Raineri, Appl. Phys. Lett. **92**, 252101 (2008).

[25] D.M. Schaadt, E.J. Miller, E.T. Yu, and J.M. Redwing, Appl. Phys. Lett. **78**, 88 (2001).

[26] K. V. Smith, E.T. Yu, J.M. Redwing, and K.S. Boutros, Appl. Phys. Lett. **75**, 2250 (1999).

[27] A. Imtiaz, T.M. Wallis, J.C. Weber, K.J. Coakley, M.D. Brubaker, P.T. Blanchard, A. Bertness, N.A. Sanford, P. Kabos, K.A. Bertness, N.A. Sanford, and P. Kabos, Appl. Phys. Lett. **104**, 263107 (2014).

[28] D.E. Sviridov, V.N. Jmerik, S. Rouvimov, D. V. Nechaev, V.I. Kozlovsky, and S. V. Ivanov, Appl. Phys. Lett. **114**, 061601 (2019).

[29] K.L. Johnson, *Contact Mechanics* (University Press: Cambridge, 1985).

[30] F. Giannazzo, V. Raineri, S. Mirabella, G. Impellizzeri, F. Priolo, M. Fedele, and R. Mucciato, J. Vac. Sci. Technol. B Microelectron. Nanom. Struct. Process. Meas. Phenom. **24**, 370 (2006).

[31] Y. Huang, C.C. Williams, and M.A. Wendman, J. Vac. Sci. Technol. A Vacuum, Surfaces, Film. **14**, 1168 (1996).

[32] T. Hantschel, M. Tsigkourakos, L. Zha, T. Nuytten, K. Paredis, B. Majeed, and W. Vandervorst, Microelectron. Eng. **159**, 46 (2016).

[33] T.D. Veal, P.H. Jefferson, L.F.J. Piper, C.F. McConville, T.B. Joyce, P.R. Chalker, L. Considine, H. Lu, and W.J. Schaff, Appl. Phys. Lett. **89**, 202110 (2006).

[34] P.D.C. King, T.D. Veal, A. Adikimenakis, H. Lu, L.R. Bailey, E. Iliopoulos, A. Georgakilas, W.J. Schaff, and C.F. McConville, Appl. Phys. Lett. **92**, 172105 (2008).

[35] K. V. Smith, X.Z. Dang, E.T. Yu, and J.M. Redwing, J. Vac. Sci. Technol. B Microelectron. Nanom. Struct. **18**, 2304 (2000).

Sample HPplus
300 nm p++ GaN
436 nm p GaN
10 nm u-GaN
5 nm LT-AlN
1 µm u-GaN
500 nm $Al_{0.08}Ga_{0.92}N$
367 nm $Al_{0.44}Ga_{0.56}N$
380 nm $Al_{0.75}Ga_{0.25}N$
200 nm AlN
Si (111)

Sample HN
1.7 µm n- GaN
350 nm u-GaN
300 nm $Al_{0.08}Ga_{0.92}N$
250 nm $Al_{0.44}Ga_{0.56}N$
250 nm $Al_{0.75}Ga_{0.25}N$
200 nm AlN
Si (111)

Sample HNplus
n++ GaN 500 nm
500 nm u-GaN
300 nm $Al_{0.08}Ga_{0.92}N$
250 nm $Al_{0.44}Ga_{0.56}N$
250 nm $Al_{0.75}Ga_{0.25}N$
200 nm AlN
Si (111)